

Synchrotron X-ray microtomography and lattice Boltzmann simulations of gas flow through volcanic pumices

Wim Degruyter¹, A. Burgisser², O. Bachmann³, and O. Malaspinas⁴

¹*Section des Sciences de la Terre et de l'Environnement, Université de Genève, 13 Rue des Maraîchers, CH-1205, Genève, Switzerland*

²*Institut des Sciences de la Terre d'Orléans, CNRS - Université d'Orléans, 1A rue de la Férollerie, 45071 Orléans Cedex 2, France*

³*Department of Earth and Space Sciences, Mailstop 351310, University of Washington, Seattle, WA 98195-1310, USA*

⁴*Laboratory of Computational Engineering, EPFL, Station 9, CH-1015, Lausanne*

ABSTRACT

To illustrate the advances made in permeability calculations combining X-ray microtomography and lattice Boltzmann method simulations, a sample suite of different types of pumices was investigated. Large three dimensional images at high spatial resolution were collected at three different synchrotron facilities (Elettra, SLS, and ESRF). Single phase gas flow simulations were done on computer clusters with a highly parallelized lattice Boltzmann code, named Palabos. Permeability measurements obtained by gas flow simulation were compared to lab measurements of pumices produced by the Kos Plateau Tuff eruption to validate the method. New permeability data for pumices from other silicic volcanic deposits is presented, and an empirical model for permeability is tested using geometrical and topological data, i.e. tortuosity, specific surface area, total and connected porosity.

22 Sep 2010 version 1
insu-00468535

INTRODUCTION

Macroscopic transport of fluids in porous media has numerous applications in various fields of geosciences (e.g. Turcotte and Schubert, 2002). Macroscopically, this transport is quantified by permeability k through Darcy's law

$$-\frac{dP}{dx} = \frac{\mu}{k} U, \quad (1)$$

with x the direction of flow, $-dP/dx$ the pressure gradient, μ the fluid viscosity, and U the average velocity per unit area. The permeability k is determined by the characteristics of the porous medium (geometry and topology) at the micro-scale. Empirical models (e.g., Kozeny-Carman equation) relate geometrical properties such as specific surface area, and channel shape together with topological quantities such as tortuosity and connected porosity quantitatively to permeability (Bear, 1972). However, different types of rock require different types of empirical equations, and therefore a detailed examination of rocks combined with model testing is needed.

Both X-ray tomographic imaging (Flannery et al., 1987), and lattice Boltzmann numerical techniques (Wolf-Gladrow, 2000; Succi, 2001; Chopard et al., 2002; Sukop and Thorne, 2006) emerged at the end of the 1980's and it was soon realized that these techniques were very compatible for permeability studies (Ferreol and Rothman, 1995, Heijs and Lowe, 1995; Auzerais et al., 1996). The lattice Boltzmann method (LBM) is excellent for modeling flow in complex geometries, and X-ray tomography provides the three dimensional (3D) geometries needed as boundary conditions for the flow. Compared to laboratory measurements, this numerical technique has the great advantage that the velocity distribution can immediately be linked to the micro-scale geometry of the porous medium. The main drawback of the method, simulating a large enough volume (Representative Elementary Volume, REV; Bear, 1972) at a high enough spatial resolution, becomes less prominent as X-ray tomography and computer

power (clusters) advance and become more available. Today, X-ray tomography facilities at synchrotron beamlines easily produce $>1024^3$ voxels of data, in combination with submicron spatial resolutions (Stampanoni et al., 2006; Weitkamp et al., in press), while lattice Boltzmann codes are highly parallelized to be able to handle such large volumes (Harting et al., 2005; Fredrich et al., 2006).

The development of permeability in the volcanic conduit during an eruption is believed to play an important role in the shift between eruptive styles (Eichelberger et al., 1986; Woods and Koyaguchi, 1994; Gonnermann and Manga, 2007; Mueller et al., 2008). Pumices (highly vesicular volcanic rock) record the state of permeability in the volcanic conduit just prior to fragmentation, provided they are quenched fast enough and are highly viscous (Thomas et al., 1994). Hence they give us insight in the degassing mechanisms during a volcanic eruption.

Here, we combine X-ray tomography with lattice Boltzmann numerical simulations of fluid transport to obtain geometrical properties and permeability estimates of pumices. In the line of previous studies (Wright et al., 2006; Polacci et al., 2009) images were obtained at very high spatial resolutions and flows were simulated on large enough grids to capture the REV. We focus on pumices produced by the Kos Plateau Tuff eruption and compare the results to published laboratory results (Bouvet de Maisonneuve et al., 2009). We also present the first permeability results for silicic pumices of five other explosive eruptions (Okmok Volcano (USA), Nevado de Toluca (Mexico), Mt Dore (France), Cappadocia (Turkey), Mt Pelée (Martinique, Lesser Antilles)). These analysis are accompanied by the quantification of geometrical and topological characteristics of the pore space, i.e. total and connected porosity, tortuosity, and specific surface area to test an empirical model suggested by Degruyter et al., 2010.

insu00488535 version 1 - 22-Sep-2010

SAMPLES

Samples from six different silicic volcanic deposits were selected for analysis. The general characteristics of each of these deposits are summarized in Table 1. The main set of samples is composed of pumices from the 160 ky B.P. Kos Plateau Tuff eruption (KPT). This eruption produced various types of pumices which were well characterized in previous studies (Allen, 2001; Bouvet de Maisonneuve et al., 2009; Degruyter et al., 2010). Tube, frothy, and microvesicular (μ Ves) pumices were used to validate the method (Figure 1). The samples were taken from the same clasts as the study of Bouvet de Maisonneuve et al., 2009. The rest of the samples were taken from Okmok volcano, Alaska (AOK; Burgisser, 2005; Larsen et al., 2007), Nevado de Toluca volcano, Mexico (ATO; Burgisser and Gardner, 2006), Cappadocia, Turkey (CAP; Druitt et al., 1995), Mt Dore, Massif Central, France (GNP; Mossand, 1983), and Mt. Pelée, Martinique, Lesser Antilles (MT ; Martel and Poussineau, 2007). From each clast, one or several 5 mm cylindrical cores were drilled as this is the most optimal shape to scan a maximum volume of the sample (Ketcham and Carlson, 2001). In total 12 samples were prepared from 9 clasts (Table 2).

X-RAY TOMOGRAPHY AND IMAGE ANALYSIS

Modern synchrotron radiation facilities produce a high flux source of monochromatic X-rays, ideally suited for micrometer and sub-micrometer 3D imaging. Together with large cameras ($\geq 1024 \times 1024$ pixels), this allows the quantification of large enough volumes of material. For this study, X-ray microtomographic imaging was performed at three different synchrotron facilities: the SYRMEP beamline at Elettra (Trieste, Italy; Polacci et al., 2009), the TOMCAT beamline at SLS (Villigen, Switzerland; Stampanoni et al., 2006), and the ID-19 beamline at ESRF (Grenoble, France; Weitkamp et al., in press). At all these facilities the beam energy was

insu-00488535 - version 1 - 22-Sep-2010

varied between 20 and 25 keV. The samples were rotated 180 degrees and between 1000 and 3000 projections were taken per scan. At the SYRMEP a Field of View (FOV) of $7.9 \times 3.7 \text{ mm}^2$, and an effective pixel size of $7.74 \times 7.74 \text{ }\mu\text{m}^2$ were used. At both the TOMCAT and the ID-19 a FOV between $0.75 \times 0.75 \text{ mm}^2$ and $1.5 \times 1.5 \text{ mm}^2$ was used with submicron effective pixel sizes between $0.37 \times 0.37 \text{ }\mu\text{m}^2$ and $0.74 \times 0.74 \text{ }\mu\text{m}^2$ (see Table 2). For the submicron scans we used the ‘local tomography’ technique to avoid reducing the size of the fragile samples (Faridani et al., 1992; Faridani et al., 1997). With this technique the camera zooms into the sample, leaving it partly outside the field of view. Noise is suppressed by rotating the sample continuously. Some of the samples were long enough in the direction perpendicular to the scan plane to capture several sub-volumes. In total 27 sub-volumes were scanned and analyzed (Table 2). The reconstruction of the images was done using the in house software developed at the respective synchrotron beamlines. All images were converted to a stack of 8-bit gray scale images, and were then cropped into cubes for further analysis (Figure 2a). Tube pumice images, for which the information was slightly tilted with respect to the z-direction, were re-aligned and re-cropped with ImageJ.

Image segmentation, the process by which a grey scale image is converted into black and white voxels, was done using the Indicator Kriging method of 3dma-rock (Oh and Lindquist, 1999) and/or the Seed threshold method of Blob3D (Ketcham, 2005) giving a stack of binary images (Figure 2b). Segmentation can introduce some errors. Hence, a post segmentation clean up is performed by removing all objects with an equivalent sphere diameter of < 3 voxels (total of 27 voxels). Therefore the accuracy of the measurements will be 3 times the effective voxel size. Volume renderings of the segmented images were done with Paraview (Figure 1). Total porosity was measured by counting the number of white voxels and dividing by the total volume.

The connected porosity was calculated in each perpendicular direction, by labeling the separated connected clusters of white voxels with ImageJ. The medial axis calculated in 3dma-rock can be used to search for the shortest paths between two end faces (Lindquist and Venkatarangan, 1999). The average of this value divided by the length between the two faces gives us the tortuosity. The surface area of the porous medium was calculated on the segmented volume with a Marching Cubes algorithm (Lorenson and Cline, 1987), which is incorporated in the 3dma-rock code. This algorithm creates triangulated surfaces from the original voxel data and therefore avoids overestimating the surface area if calculated directly from the voxel surfaces. Dividing this by the total volume gives the specific surface area. Total porosity, tortuosity, and specific surface area are listed in Table 3. All connected porosities were found to be within 3% of the total porosity.

LATTICE-BOLTZMANN METHOD AND COMPUTER RESOURCES

Lattice Boltzmann simulations were carried out using Palabos (Latt, 2009). Palabos is an open-source software for computational fluid dynamics using the LBM. As it is highly flexible and parallel, it can handle a wide variety of fluid dynamics problems. The LBM itself has been thoroughly described and validated in the literature (Wolf-Gladrow, 2000; Succi, 2001; Chopard et al., 2002; Sukop and Thorne, 2006). In this study, a single phase gas flow is simulated through the obtained 3D images. Using the segmented images as input data, the walls of the porous medium are converted to bounce-back boundary conditions. The geometries were padded with walls in the direction perpendicular to flow in order to eliminate the need for periodic boundaries. The standard BGK collision operator is applied with a D3Q19 lattice. Initially the fluid velocity is set to zero and fluid movement is induced by holding a fixed pressure gradient between the inlet and outlet. Steady state is reached when the standard deviation of the average

energy, as measured over a fixed number of time steps, falls below a given threshold value (we chose 1000 time steps, and a threshold value of 10^{-4}). To ensure the flow was in the laminar regime ($Re \ll 1$), it was checked if the permeability stayed constant when the applied pressure gradient was varied over several orders of magnitude. Furthermore, as discussed by Ferreol and Rothman, 1995, the channels through which the fluid flows must be sufficiently resolved to avoid non hydrodynamic effects. This was verified by refining the grid of parts of the analyzed volumes and checking that the permeability stayed constant for these refinements. The code is available at the Palabos website with a tutorial (Latt, 2009).

Steady state results of the model are analyzed to obtain permeability. From the velocity distribution throughout the 3D volume equation (1) is used together with the given pressure gradient and fluid viscosity to solve for permeability k in non dimensional lattice units. This value is easily converted to real world units by multiplying with the square of the effective length of a voxel side. For each volume three permeability values are obtained, one in each orthogonal direction (in total 79 points; Table 3). Figure 2 shows the steps from a cropped gray-scale image (A) to binary image (B) and finally to a velocity distribution simulated with the LBM (C) for a slice of sample AOK1A. Figure 3 shows the complex streamlines of the flow through frothy pumice (KPT32c). Alternatively, these streamlines can be used for tortuosity calculations (e.g. Matyka et al., 2008).

A large amount of memory needs to be allocated for the volumes that are analyzed. Therefore simulations were run on several computer clusters: Myrinet (University of Geneva, Switzerland, 32 nodes, 2 processors, and 2Gb RAM per node), Atlas (Georgia Tech, Atlanta, USA, 128 nodes, 8 processors, and 8Gb RAM per node), Phoebus (CNRS, Orleans, France, 42 nodes, 8 processors, and 8Gb RAM per node), Cadmos (EPFL, Lausanne, Switzerland, 4000

nodes, 4 processors, and 4 Gb RAM per node). Between 8 and 128 processors were used for each simulation, except on Cadmos where 2048 processors were used, and a run took between 10 and 30 hours.

RESULTS

Effect of resolution and analyzed volume on measurements

Following Zhang et al., 2000 we demonstrate the need of having a REV at high enough spatial resolution for adequate characterization of a porous medium on sample AOK1A. To test spatial resolution effects the segmented volume is rescaled by transforming each $2 \times 2 \times 2$ voxels to 1 voxel with a certain rule. Here two different rules are applied: if the $2 \times 2 \times 2$ voxels have more than 4 white voxels it is converted to 1 white voxel, otherwise it becomes black (Rule 1), if the $2 \times 2 \times 2$ voxels have more than 7 white voxels it is converted to 1 white voxel, otherwise it becomes black (Rule 2). For Rule 1 the wall become less resolved with increasing the effective voxel size, while for Rule 2 it is the bubble network that loses resolution. Hereby we artificially increase the effective voxel size from $0.55^3 \mu\text{m}^3$, over $1.1^3 \mu\text{m}^3$, $2.2^3 \mu\text{m}^3$, and $4.4^3 \mu\text{m}^3$ to $8.8^3 \mu\text{m}^3$, while maintaining the actual size of the analyzed volume. The effect of losing resolution is demonstrated in Figure 4: Rule 1 results in increasing permeability and connected porosity, while Rule 2 has the opposite effect. For this example the decrease in spatial resolution becomes significant at an effective voxel size of $2.2^3 \mu\text{m}^3$. Note that the deviation of the connected porosity is solely due to misrepresentation of the solid-void space, while that of the permeability can arise from both the misrepresentation of the solid-void space and numerical errors induced by not resolving the flow in the channels properly (Ferreol and Rothman, 1995). To find the REV the original segmented volume of 1024^3 voxels is divided into 8 subvolumes of 512^3 voxels, while maintaining the effective pixel size of $0.55^3 \mu\text{m}^3$. Then a subvolume of 512^3 voxels

is selected around the center point of the original volume, and is again divided into 8 subvolumes of 256^3 voxels. This procedure is repeated until we reached 8 volumes of 64^3 voxels. The effect of losing volume on permeability and connected porosity is demonstrated in Figure 5. For this example the loss of volume becomes significant at a volume of 256^3 voxels.

Validation of the method on KPT samples

The permeability measurements done with LBM simulations compare well with laboratory measurements done on KPT samples (Bouvet de Maisonneuve et al., 2009; Figure 6A and B). Laboratory measurements were done on $\sim (25 \text{ mm})^3$ volumes while volumes analyzed here varied between $(0.37 \text{ mm})^3$ and $(2.5 \text{ mm})^3$. Despite this vast volume difference of 4-6 orders of magnitude similar spreads within the same pumice type and in between pumice types are found. This remarkable agreement between simulated and measured permeability shows that 1) the tomographic volumes qualify as REV's and 2) the pumices were imaged at a high enough spatial resolution. In fact, the points with the greatest mismatch (i.e. frothy type) are also the smallest grids analyzed (Table 2). This shows the necessity of doing large scale simulations ($> 12^3$ voxels) to be within the REV (Zhang et al., 2000).

Tortuosity has a clear influence on permeability of volcanic rocks (Le Pennec et al., 2001; Bernard et al., 2007; Wright et al., 2009). The trends in Figure 7A and C confirm qualitative conclusions of previous studies (Bouvet de Maisonneuve et al., 2009; Degruyter et al., 2010). The frothy pumice has a higher tortuosity leading to a lower permeability than tube measured parallel to vesicle elongation despite its higher porosity. The anisotropic permeability within tube pumice is also clearly influenced by tortuosity differences caused by bubble elongation. The μVes pumice is characterized by having a relatively low tortuosity and low permeability. This is explained by the specific surface area measurements, which scales inversely

with permeability (Saar and Manga, 1999), showing one order of magnitude difference between μ Ves and the other pumice types (Table 3).

Other deposits

Very large volumes of 1024^3 voxels ($>$ one billion grid points) were analyzed for samples from the other deposits (Table 2). Qualitative inspection of the scans ensured there were enough connected bubbles per analyzed volume except for the GNP sample. Although more data is needed for each deposit, these results shed a first light on the permeability development during these eruptions (Figure 6C). A wide scatter can be observed in between the deposits as well as within the same deposit, similar to other studies (Mueller et al., 2005; Gonnermann and Manga, 2007). AOK and CAP show the influence of the bubble deformation as the permeability measured parallel to vesicle elongation is higher than the one measured perpendicular to vesicle elongation. Also GNP samples showed high deformation, but no connections perpendicular to vesicle elongation were found for these samples confirming we did not scan a REV for this sample (Table 3). Lastly the ATO and MT sample show isotropic permeability similar to KPT rothy and μ Ves pumices. Similar tortuosity-permeability trends can be observed for samples from the other deposits (figure 7B and D), as the pumice with deformed bubble networks (AOK, CAP) have a larger spread than pumices with no distinct bubble deformation (ATO, MT). The GNP data point plots in the range of the KPT tube pumice measured parallel to vesicle elongation.

DISCUSSION

This study was designed to improve existing permeability models, which use a power law relationship between porosity ϕ and permeability,

$$k=C\phi^m, \quad (2)$$

with C and m fitting constants (e.g. Klug and Cashman, 1996; Blower, 2001; Mueller et al., 2005). More sophisticated models can be presented if the fitting constants can be understood better. Previous studies have shown that the cementation factor m can be correlated with tortuosity τ and connected porosity ϕ_c using Archie's law ($\tau^2 = \phi_c^{-m}$), and C is related to the square of a characteristic length scale d of the porous medium (Costa, 2006; Bernard et al., 2007; Degruyter et al., 2010). A model used by Degruyter et al., 2010 replaces all fitting constants with measurable quantities:

$$k = \frac{\phi_c^m d^2}{32}. \quad (3)$$

As this is an equivalent channel model, only the connected porosity ϕ_c is considered, and d is the equivalent channel diameter. Length scales such as the average diameter of bubble apertures (e.g. Blower, 2001) can be used to estimate the equivalent channel diameter. Here we use the specific surface area as a length scale, which is related to the channel diameter as $d=4\phi_c/s$. Applied to (3) we get

$$k = \frac{\phi_c^{m+2}}{2s^2}. \quad (4)$$

We obtained a range for m , by combining the tortuosity, and the connected porosity data (Archie's law; Figure 5), which are comparable to results of Wright et al., 2009. Permeability was predicted with equation (3) and compared with the simulated permeability (Figure 8). Ranges predicted by the empirical model (eq. 3) compare reasonably well with observed values. Omitting rigid fitting constants allows this simple model to separate different types of pumices as well as detecting anisotropic features, providing a reasonable way to estimate permeability. Further refinement of the model can be achieved, e.g. by adding the influence of channel shape (Mortensen et al., 2005), or investigating the applicability of Archie's law (Matyka et al., 2008).

CONCLUDING REMARKS

Obtaining rock permeability data is fundamental in many areas of geosciences. 3D quantification of a porous medium is an absolute necessity to understand flow transport. As one might be able to estimate geometrical quantities such as specific surface area and porosity from 2D data, it is evident that important topological quantities of the medium like connectivity and tortuosity can not be determined in such a way. As demonstrated by Figures 2 and 3 (and the supplemental material) gas transport is governed by only a few dominant connected channels. Therefore, only a small part of the porosity will govern gas loss in pumices. Moreover the data in Figure 7 suggest an important control of tortuosity on permeability. X-ray microtomography imaging and LBM numerical simulations are becoming robust and accessible tools to deal with this issue as problems with spatial resolution and REV become negligible. The availability of open-source software such as 3dma-rock, Blob3d, ImageJ, Paraview, and Palabos will allow this method to become widely used and combine with lab measurements to build large permeability databases.

In order to obtain a realistic description of the development of permeability in the volcanic conduit, a thorough understanding of the controlling parameters, i.e. connected porosity, tortuosity, and specific surface area (or a similar length scale) is necessary, and it is clear that these properties are determined by complex dynamics of bubble growth, deformation, and coalescence (Gonnermann and Manga, 2007). More concretely, questions on (a) how the connected porosity is related to the total porosity (e.g. Burgisser and Gardner, 2004; Takeuchi et al., 2009), (b) how the tortuosity is related to deformation (e.g. Scholes et al., 2007), and (c) how dominant connected channels develop, need further investigation.

ACKNOWLEDGMENTS

This work would not have been possible without the excellent assistance at the various synchrotron beamlines. We are very grateful to Lucia Mancini, and Nicola Sodini (SYRMEP, Elettra), Christoph Hintermüller (TOMCAT, SLS), and Timm Weitkamp (ID-19, ESRF). We also like to thank Margherita Polacci for supporting this project, and assisting at the SYRMEP beamline. We counted on the expertise of Jonas Latt on using Palabos. For the use of the computer clusters we thank Josef Dufek (Atlas), Bastien Chopard and Christian Clemançon (Cadmos), and Nicolas Mayocourt (Myrinet). KPT samples and lab data were provided by Caroline Bouvet de Maisonneuve, CAP and GNP samples by Jean-Louis Bourdier, and the MT sample by Caroline Martel. WD was supported by the Swiss NSF grant #200021-111709/1. Reviews by Don Baker and two anonymous reviewers improved the manuscript.

REFERENCES CITED

- Allen, S.R., 2001, Reconstruction of a major caldera-forming eruption from pyroclastic deposit characteristics: Kos Plateau Tuff, eastern Aegean Sea: *J Volcanol Geotherm Res*, v. 105, p. 141-162.
- Buzerais, F.M., Dunsmuir, J., Ferreol, B.B., Martys, N., Olson, J., Ramakrishnan, T.S., Rothman, D.H., and Schwartz, L.M., 1996, Transport in sandstone: A study based on three dimensional microtomography: *Geophysical Research Letters*, v. 23, p. 705-708.
- Bear, J., 1972, *Dynamics of fluids in porous media*: New York, Dover.
- Bernard, M.L., Zamora, M., Geraud, Y., and Boudon, G., 2007, Transport properties of pyroclastic rocks from Montagne Pelee volcano (Martinique, Lesser Antilles): *J Geophys Res*, v. 112, p. B05205.
- Blower, J.D., 2001, Factors controlling permeability-porosity relationships in magma: *Bull Volcanol*, v. 63, p. 497-504.
- Bouvet de Maisonneuve, C., Bachmann, O., and Burgisser, A., 2009, Characterization of juvenile pyroclasts from the Kos Plateau Tuff (Aegean Arc): insights into the eruptive dynamics of a large rhyolitic eruption: *Bulletin of Volcanology*, v. 71, p. 643-658.
- Burgisser, A., 2005, Physical volcanology of the 2,050 BP caldera-forming eruption of Okmok volcano, Alaska: *Bulletin of Volcanology*, v. 67, p. 497-525.
- Burgisser, A., and Gardner, J.E., 2004, Experimental constraints on degassing and permeability in volcanic conduit flow: *Bulletin of Volcanology*, v. 67, p. 42-56.
- , 2006, Using hydraulic equivalences to discriminate transport processes of volcanic flows: *Geology*, v. 34, p. 157-160.

- Chopard, B., Dupuis, A., Masselot, A., and Luthi, P., 2002, Cellular Automata and Lattice Boltzmann techniques: an approach to model and simulate complex systems: *Adv Compl Sys*, v. 5, p. 103-246.
- Costa, A., 2006, Permeability-porosity relationship: A reexamination of the Kozeny-Carman equation based on a fractal pore-space geometry assumption: *Geophys Res Lett*, v. 33, p. L02318.
- Degruyter, W., Bachmann, O., and Burgisser, A., 2010, Controls on magma permeability in the volcanic conduit during the climactic phase of the Kos Plateau Tuff eruption (Aegean Arc): *Bulletin of Volcanology*, v. 72, p. 63-74.
- Druitt, T.H., Brenchley, P.J., Gokten, Y.E., and Francaviglia, V., 1995, Late Quaternary Rhyolitic Eruptions from the Acigol Complex, Central Turkey: *Journal of the Geological Society*, v. 152, p. 655-667.
- Eichelberger, J.C., Carrigan, C.R., Westrich, H.R., and Price, R.H., 1986, Non-explosive silicic volcanism: *Nature*, v. 323, p. 598-602.
- Faridani, A., Finch, D.V., Ritman, E.L., and Smith, K.T., 1997, Local tomography .2.: *Siam Journal on Applied Mathematics*, v. 57, p. 1095-1127.
- Faridani, A., Ritman, E.L., and Smith, K.T., 1992, Local Tomography: *Siam Journal on Applied Mathematics*, v. 52, p. 459-484.
- Farrel, B., and Rothman, D.H., 1995, Lattice-Boltzmann Simulations of Flow-through Fontainebleau Sandstone: *Transport in Porous Media*, v. 20, p. 3-20.
- Flannery, B.P., Deckman, H.W., Roberge, W.G., and Damico, K.L., 1987, 3-Dimensional X-Ray Microtomography: *Science*, v. 237, p. 1439-1444.
- Fredrich, J.T., Digiovanni, A.A., and Noble, D.R., 2006, Predicting macroscopic transport properties using microscopic image data: *Journal of Geophysical Research-Solid Earth*, v. 111, p. -.
- Gonnermann, H.M., and Manga, M., 2007, The fluid mechanics inside a volcano: *Annu Rev Fluid Mech*, v. 39, p. 321-356.
- Garting, J., Chin, J., Venturoli, M., and Coveney, P.V., 2005, Large-scale lattice Boltzmann simulations of complex fluids: advances through the advent of computational Grids: *Philosophical Transactions of the Royal Society a-Mathematical Physical and Engineering Sciences*, v. 363, p. 1895-1915.
- Geijs, A.W.J., and Lowe, C.P., 1995, Numerical Evaluation of the Permeability and the Kozeny Constant for 2 Types of Porous-Media: *Physical Review E*, v. 51, p. 4346-4352.
- Ketcham, R.A., 2005, Computational methods for quantitative analysis of three-dimensional features in geological specimens: *Geosphere*, v. 1.
- Ketcham, R.A., and Carlson, W.D., 2001, Acquisition, optimization and interpretation of X-ray computed tomographic imagery: applications to the geosciences: *Computers & Geosciences*, v. 27, p. 381-400.
- Klug, C., and Cashman, K.V., 1996, Permeability development in vesiculating magmas: Implications for fragmentation: *Bull Volcanol*, v. 58, p. 87-100.
- Larsen, J.F., Neal, C., Schaefer, J., Beget, J., and Nye, C., 2007, Late Pleistocene and Holocene caldera-forming eruptions of Okmok caldera, Aleutian Islands, Alaska, Volcanism and Subduction: The Kamchatka region: *Geophysical Monograph, American Geophysical Union*, v. 172, p. 324-364.
- Latt, J., 2009, Palabos, Parallel Lattice Boltzmann Solver: <http://www.lbmethod.org/palabos/>, October, 2009.

- Le Pennec, J.L., Hermitte, D., Dana, I., Pezard, P., Coulon, C., Cocheme, J.J., Mulyadi, E., Ollagnier, F., and Revest, C., 2001, Electrical conductivity and pore-space topology of Merapi lavas: implications for the degassing of porphyritic andesite magmas: *Geophys Res Lett*, v. 28, p. 4283-4286.
- Lindquist, W.B., and Venkatarangan, A., 1999, Investigating 3D geometry of porous media from high resolution images: *Phys Chem Earth Part A* v. 24, p. 593-599.
- Lorensen, W.E., and Cline, H.E., 1987, Marching Cubes: A high resolution 3D surface construction algorithm: *Computer Graphics*, v. 21, p. 163-169.
- Martel, C., and Poussineau, S., 2007, Diversity of eruptive styles inferred from the microlites of Mt Pelee andesite (Martinique, Lesser Antilles): *Journal of Volcanology and Geothermal Research*, v. 166, p. 233-254.
- Matyka, M., Khalili, A., and Koza, Z., 2008, Tortuosity-porosity relation in porous media flow: *Physical Review E*, v. 78, p. -.
- Mortensen, N.A., Okkels, F., and Bruus, H., 2005, Reexamination of Hagen-Poiseuille flow: Shape dependence of the hydraulic resistance in microchannels: *Phys Rev E*, v. 71.
- Mossand, P., 1983, Le volcanisme anté et syn-caldera des Monts Dore [PhD thesis], University of Clermont Ferrand.
- Mueller, S., Melnik, O., Spieler, O., Scheu, B., and Dingwell, D.B., 2005, Permeability and degassing of dome lavas undergoing rapid decompression: An experimental determination: *Bull Volcanol*, v. 67, p. 526-538.
- Mueller, S., Scheu, B., Spieler, O., and Dingwell, D.B., 2008, Permeability control on magma fragmentation: *Geology*, v. 36, p. 399-402.
- Oh, W., and Lindquist, W.B., 1999, Image thresholding by indicator kriging: *Ieee Transactions on Pattern Analysis and Machine Intelligence*, v. 21, p. 590-602.
- Polacci, M., Baker, D.R., Mancini, L., Favretto, S., and Hill, R.J., 2009, Vesiculation in magmas from Stromboli and implications for normal Strombolian activity and paroxysmal explosions in basaltic systems: *Journal of Geophysical Research-Solid Earth*, v. 114, p. -.
- Saar, M.O., and Manga, M., 1999, Permeability-porosity relationship in vesicular basalts: *Geophys Res Lett*, v. 26, p. 111-114.
- Scholes, O.N., Clayton, S.A., Hoadley, A.F.A., and Tiu, C., 2007, Permeability anisotropy due to consolidation of compressible porous media: *Transp Porous Med*, v. 68, p. 365-387.
- Stampanoni, M., Groso, A., Isenegger, A., Mikuljan, G., Chen, Q., Bertrand, A., Henein, S., Betemps, R., Frommherz, U., Böhler, P., Meister, D., Lange, M., and Abela, R., 2006, Trends in synchrotron-based tomographic imaging: the SLS experience: *Proceedings of SPIE*, v. 6318, p. 63180M.
- Succi, S., 2001, *The lattice Boltzmann equation for fluid dynamics and beyond*: Oxford, Oxford University Press.
- Sukop, M.C., and Thorne, D.T., 2006, *Lattice Boltzmann Modeling: An introduction for geoscientists and engineers*: Berlin, Springer, 172 p.
- Takeuchi, S., Tomiya, A., and Shinohara, H., 2009, Degassing conditions for permeable silicic magmas: Implications from decompression experiments with constant rates: *Earth and Planetary Science Letters*, v. 283, p. 101-110.
- Thomas, N., Jaupart, C., and Vergnolle, S., 1994, On the Vesicularity of Pumice: *Journal of Geophysical Research-Solid Earth*, v. 99, p. 15633-15644.
- Turcotte, D.L., and Schubert, G., 2002, *Geodynamics*, Cambridge University Press.

- Weitkamp, T., Tafforeau, P., Boller, E., Cloetens, P., Valade, J.-P., Bernard, P., Peyrin, F., Ludwig, W., Helfen, L., and Baruchel, J., in press, Status and evolution of the ESRF beamline ID19: AIP Conference Proceedings.
- Wolf-Gladrow, D.A., 2000, Lattice-Gas Cellular Automata and Lattice Boltzmann Models: An Introduction: Berlin, Springer-Verlag.
- Woods, A.W., and Koyaguchi, T., 1994, Transitions between Explosive and Effusive Eruptions of Silicic Magmas: *Nature*, v. 370, p. 641-644.
- Wright, H.M.N., Cashman, K.V., Gottesfeld, E.H., and Roberts, J.J., 2009, Pore structure of volcanic clasts: Measurements of permeability and electrical conductivity: *Earth and Planetary Science Letters*, v. 280, p. 93-104.
- Wright, H.M.N., Roberts, J.J., and Cashman, K.V., 2006, Permeability of anisotropic tube pumice: Model calculations and measurements: *Geophysical Research Letters*, v. 33, p. -.
- Zhang, D.X., Zhang, R.Y., Chen, S.Y., and Soll, V.E., 2000, Pore scale study of flow in porous media: Scale dependency, REV, and statistical REV: *Geophysical Research Letters*, v. 27, p. 1195-1198.

FIGURE CAPTIONS

Figure 1: Volume renderings of segmented images reveal the different types of bubble network structures (white) within the porous medium (black). (A) Frothy, sample KPT27C, (B) Tube, sample KPT54A1, (c) μ Ves, sample KPT43G1. To appreciate the difference in scale, figures (B) and (C) are put as insets in figure (A).

Figure 2: Steps of image processing applied on sample AOK1A (slices perpendicular to z direction). Cropped gray scale image slice 1024x1024 pixels (A), binary image (B), velocity distribution of flow perpendicular to the slice (C). The color scale depicts the normalized velocity magnitude at each point in the domain with blue minimum velocity, red maximum velocity, and black shows the pumice walls.

Figure3: (A) 3D velocity distribution within a frothy pumice (KPT32c, flow in x-direction from $x=0$ to $x=399$) showing the heterogeneity of porous media flow. Fluid transport is dominated by only a couple of channels. (B) Streamlines show the tortuous fluid trajectory through the largest channel. All quantities are in non-dimensional lattice units. Movies showing the rotation of these 3D figures can be found in the Supplemental Material.

Figure 4: The effect of changing effective voxel size on permeability and connected porosity for sample AOK1A. The black data points indicate the starting value in the x, y, and z direction for an effective voxel size of $0.55^3 \mu\text{m}^3$. For Rule 1 by which the walls of the pumice become less resolved the connected porosity and permeability increases when the effective voxel size increases to $1.1^3 \mu\text{m}^3$, $2.2^3 \mu\text{m}^3$, $4.4^3 \mu\text{m}^3$ and $8.8^3 \mu\text{m}^3$. For Rule 2 by which the void space of the pumice becomes less resolved the connected porosity and permeability decreases when the effective voxel size increases to $1.1^3 \mu\text{m}^3$, $2.2^3 \mu\text{m}^3$, $4.4^3 \mu\text{m}^3$ and $8.8^3 \mu\text{m}^3$. In the y direction the connected porosity becomes 0 at $8.8^3 \mu\text{m}^3$, while in the x direction it becomes 0 at $4.4^3 \mu\text{m}^3$.

Rule 1 has a stronger effect on permeability than connected porosity, while Rule 2 has a stronger effect on connected porosity than permeability. Both rules show a clear deviation from the starting values at an effective voxel size of $2.2^3 \mu\text{m}^3$.

Figure 5: The effect of changing the analyzed volume on permeability and connected porosity for sample AOK1A in the x-direction (A), the y-direction (B), and the z-direction (C). The values of the original volume of 1024^3 voxels are indicated with 1024. The average values with error bars of 1 standard deviation are shown for the volumes of 512^3 , 256^3 , 128^3 and 64^3 voxels. In all direction volumes of 256^3 voxels show large error bars indicating that this volume sizes no longer provide a REV.

Figure 6: Porosity versus permeability plots for all analyzed volumes. The symbols represent the measurements for the simulations and the light colored areas surround the laboratory measurements of Bouvet de Maisonneuve et al. 2009: (A) KPT tube pumice parallel (\parallel), and perpendicular (\perp) to bubble elongation, and frothy pumices, (B) microvesicular (μVes) pumices, and (C) AOK, ATO, CAP, GNP, and MT pumice. One point of the frothy pumice permeability falls far from the laboratory data.

Figure 7: Tortuosity-permeability plots for KPT samples (A) and other deposits (B), and connected porosity- tortuosity plots for the KPT (C) and other deposits (D). Symbols are as in Figure 4.

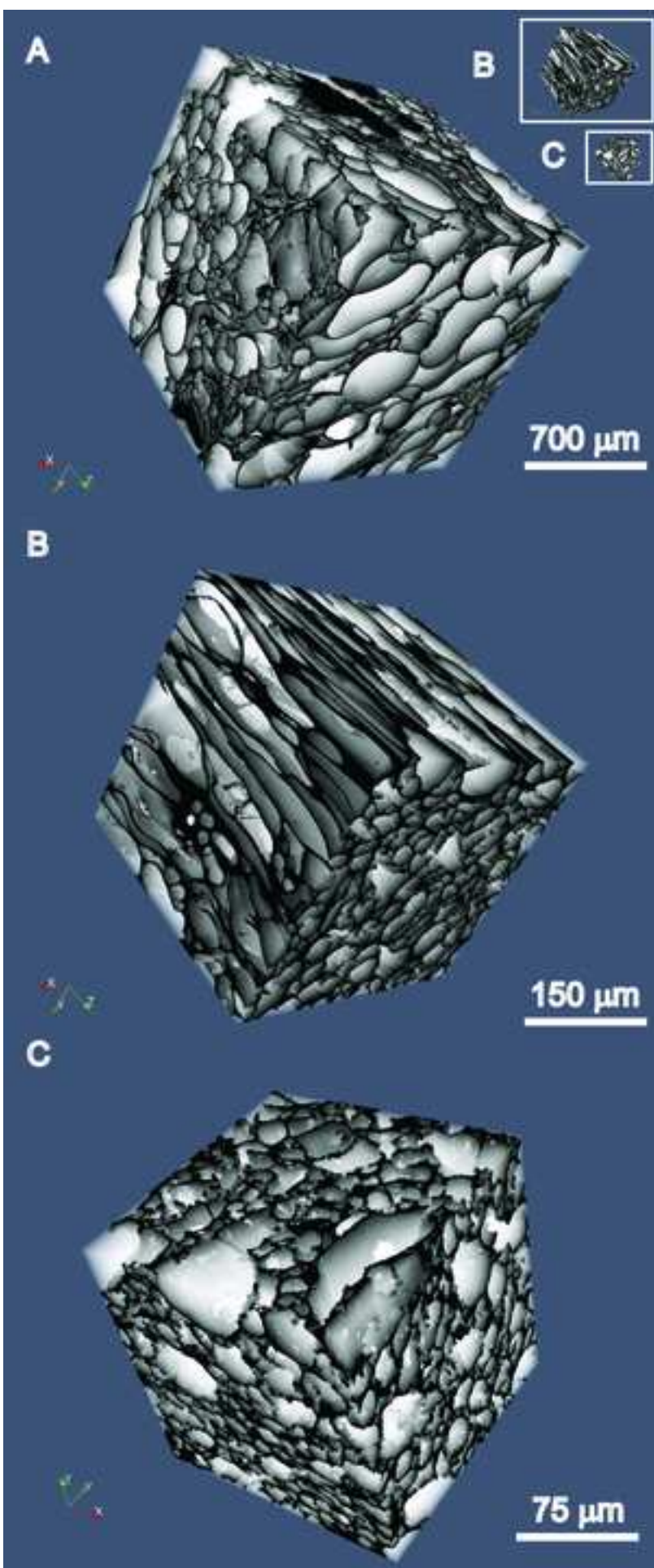
Figure 8: Comparison of observed permeability (boxes; Table 3) and prediction by empirical model (arrows; eq. (4)).

TABLE CAPTIONS

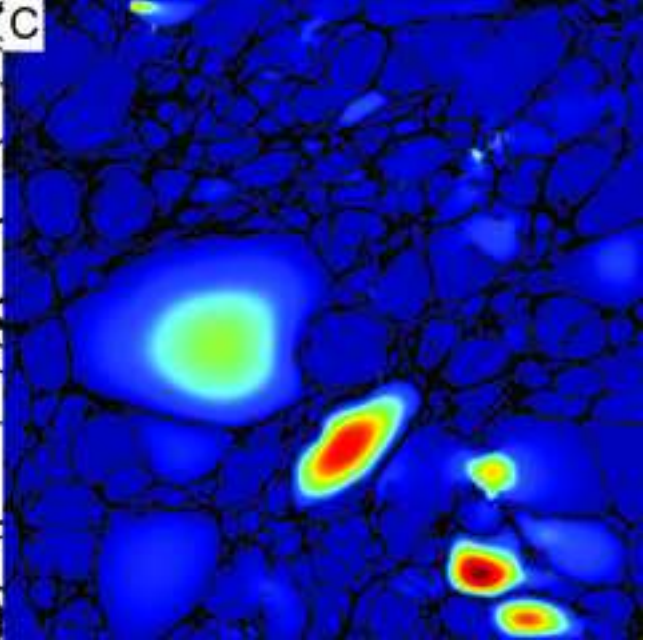
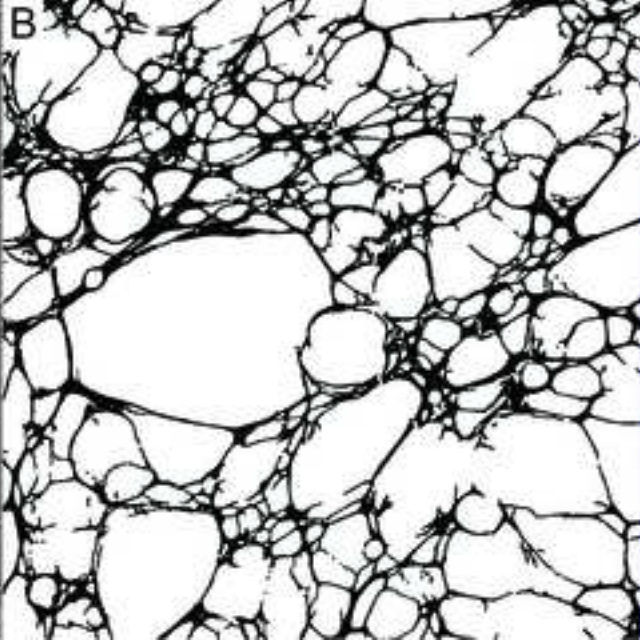
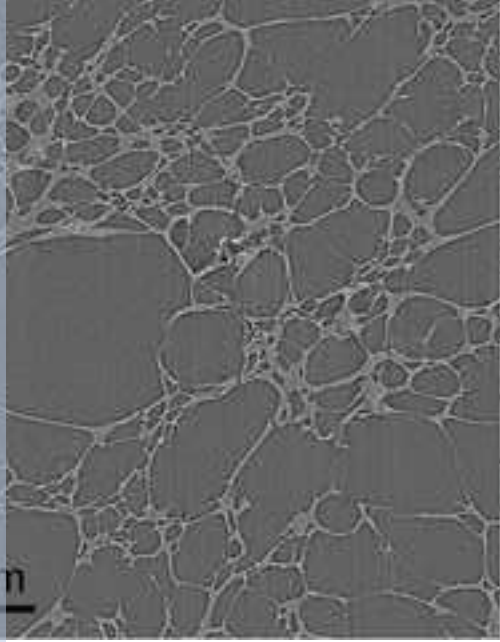
Table1: List of eruptions from which the investigated samples originate.

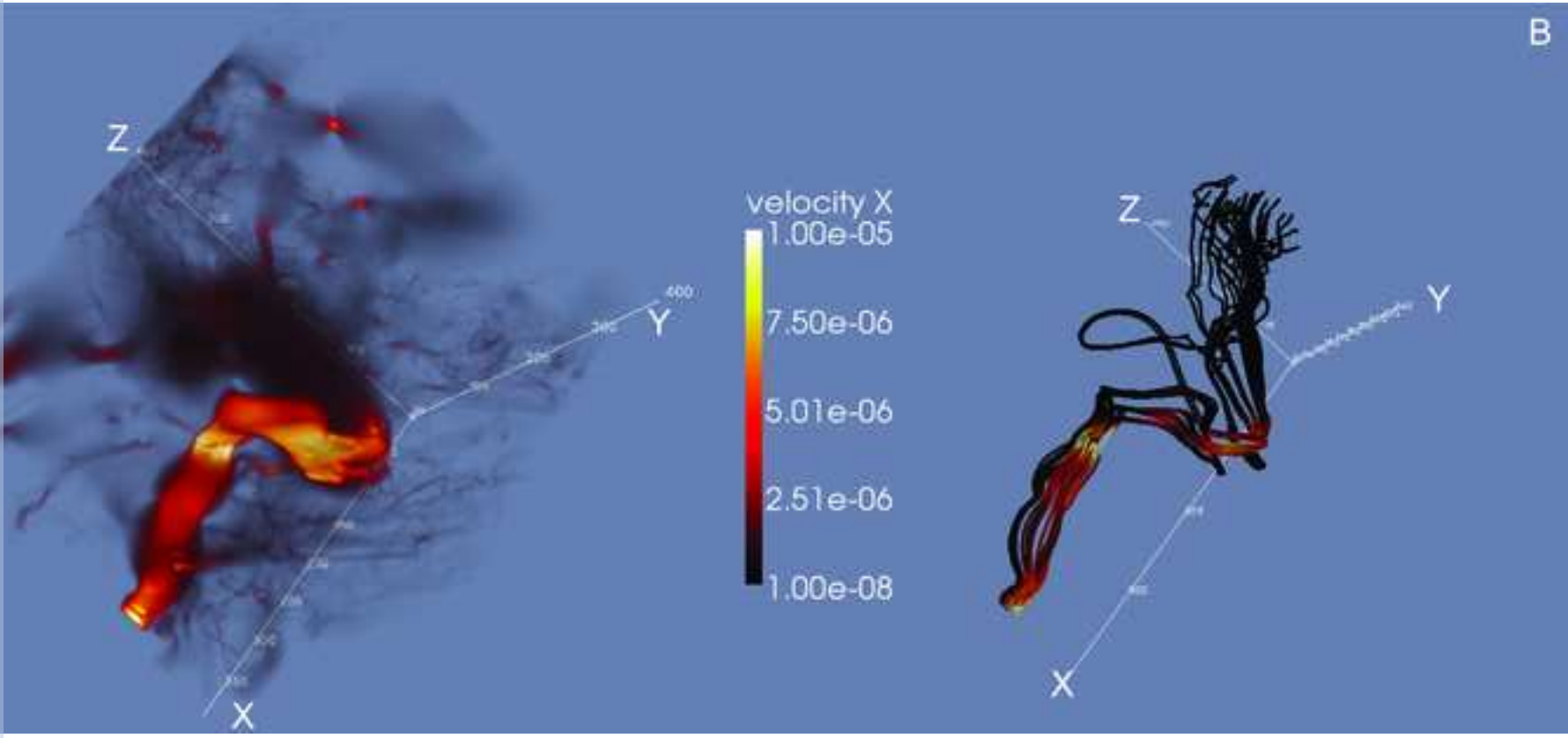
Table 2: List of investigated samples.

Table 3: List of results. Measurements of total porosity ϕ , tortuosity in each orthogonal direction of the 3D volume τ_z, τ_x, τ_y , permeability in each orthogonal direction of the 3D volume k_z, k_x, k_y (m^2), and the specific surface area and s (1/m).

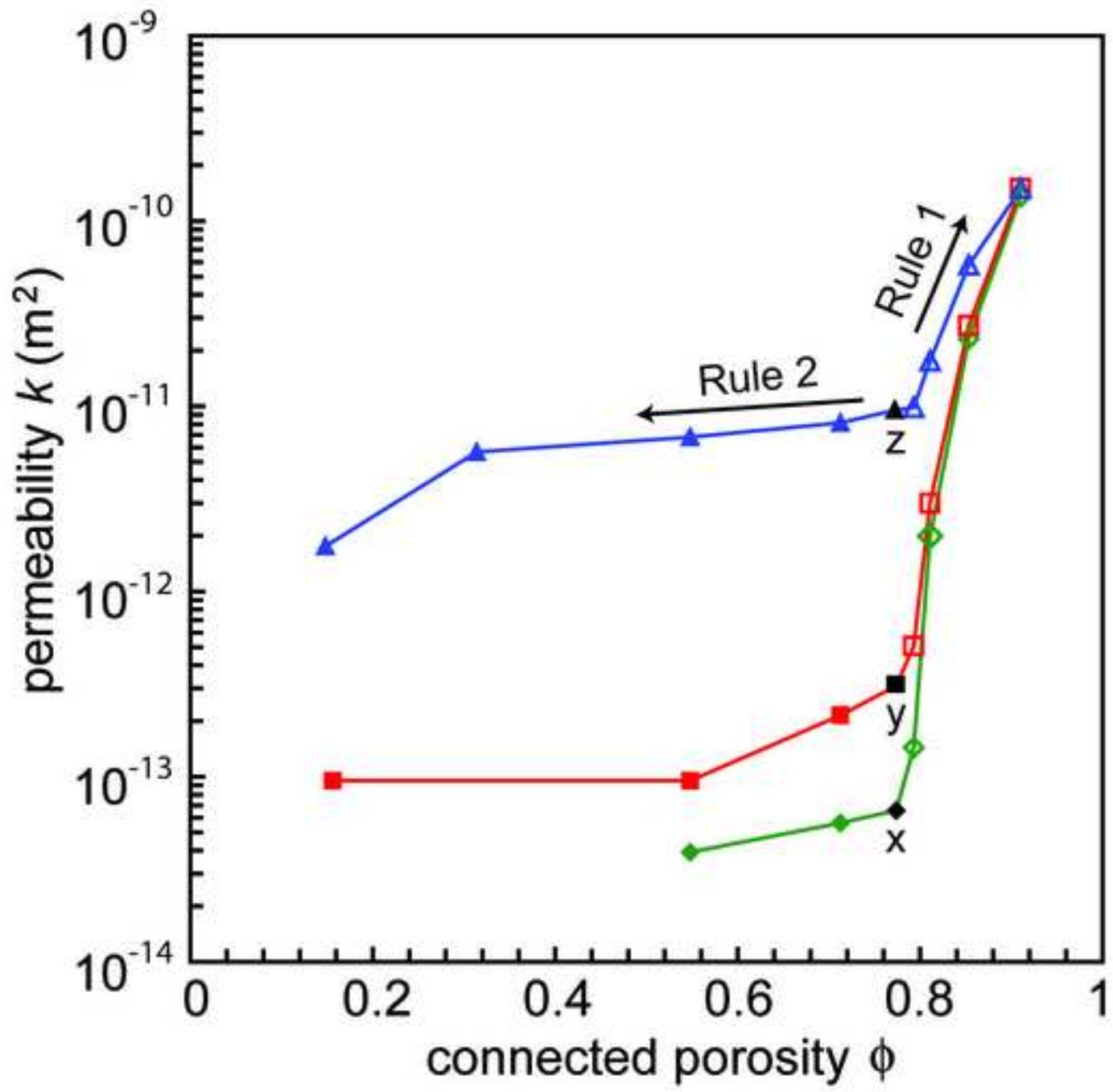


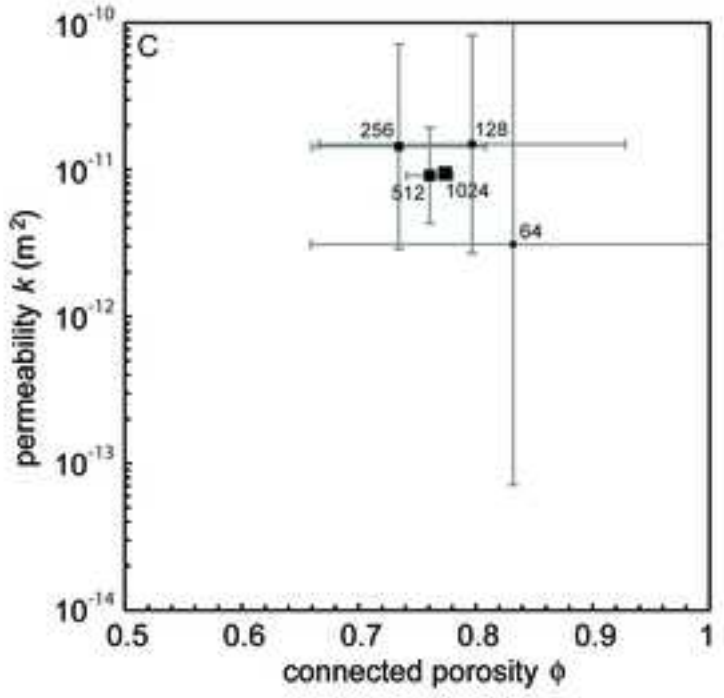
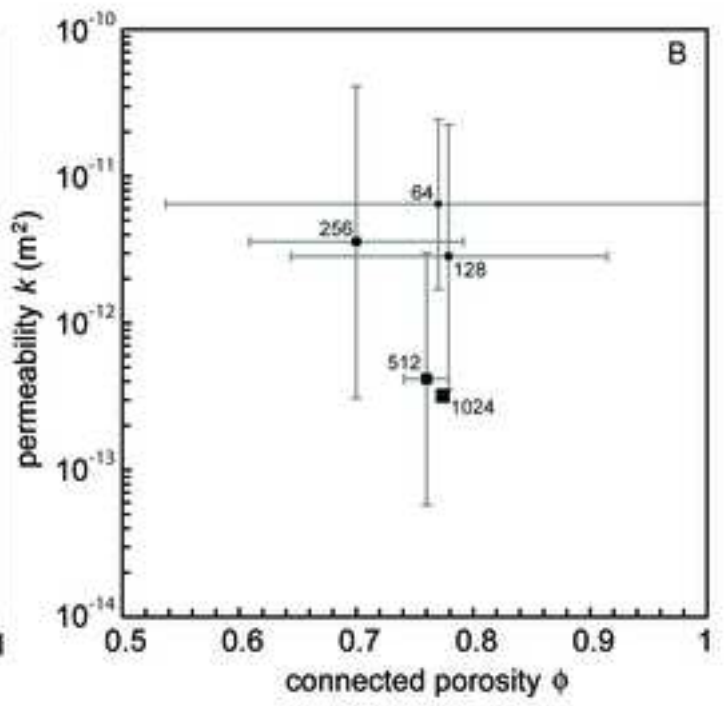
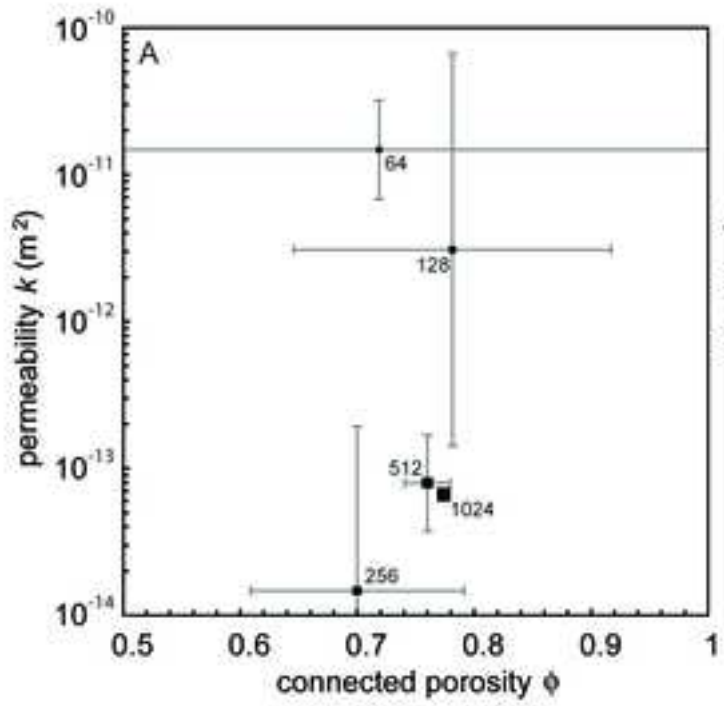
0 μ m

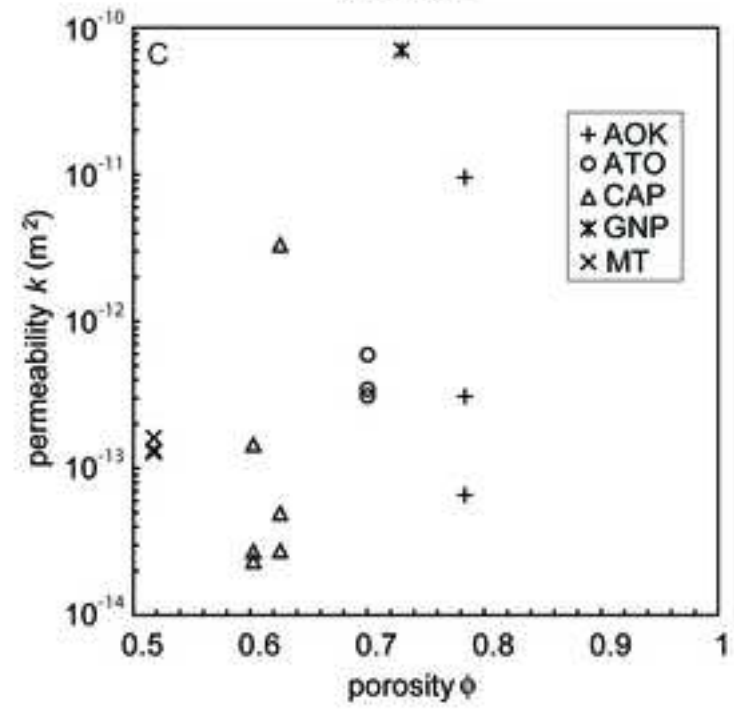
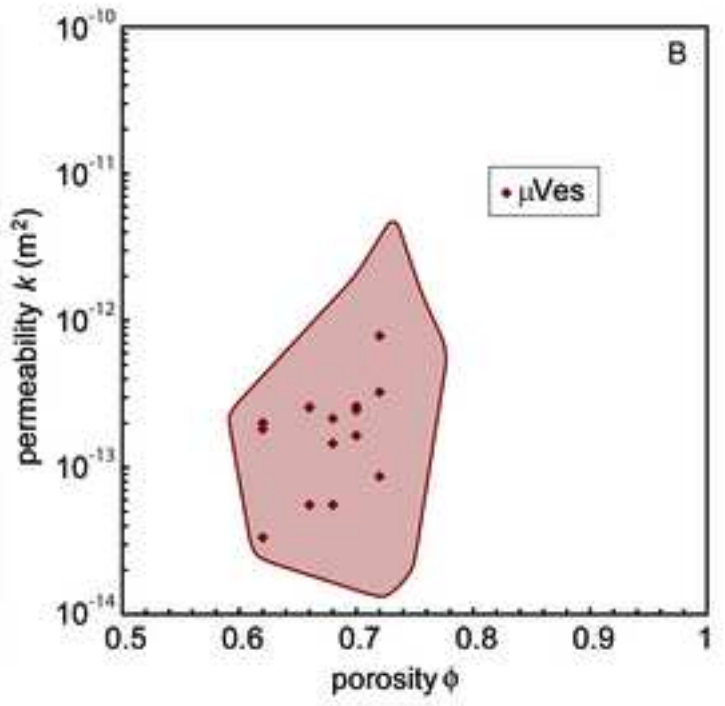
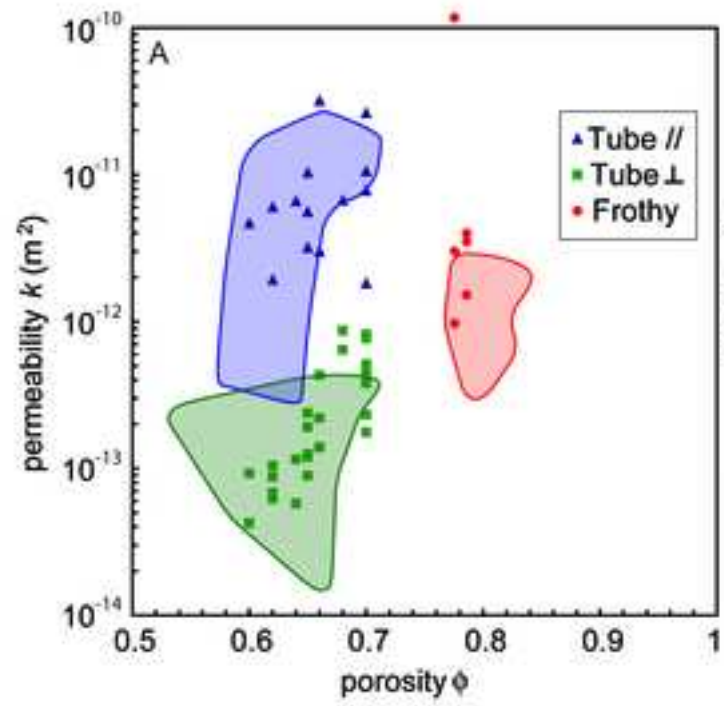


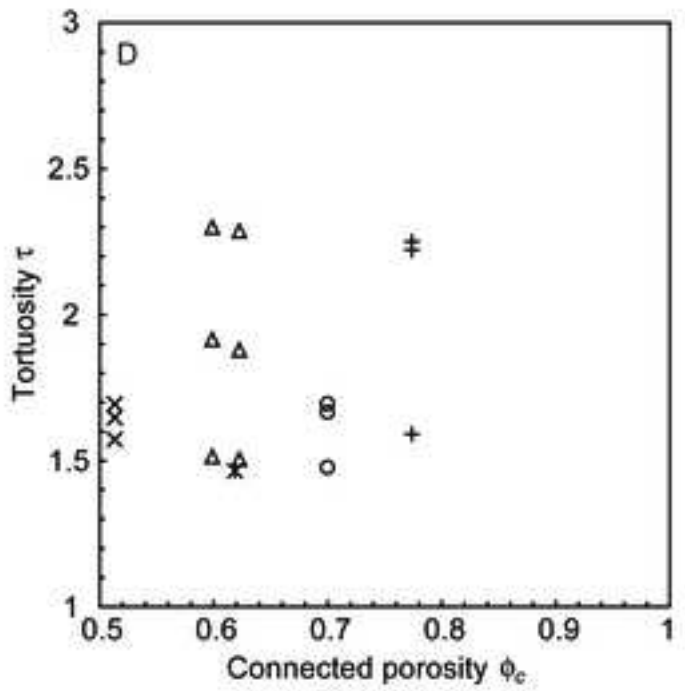
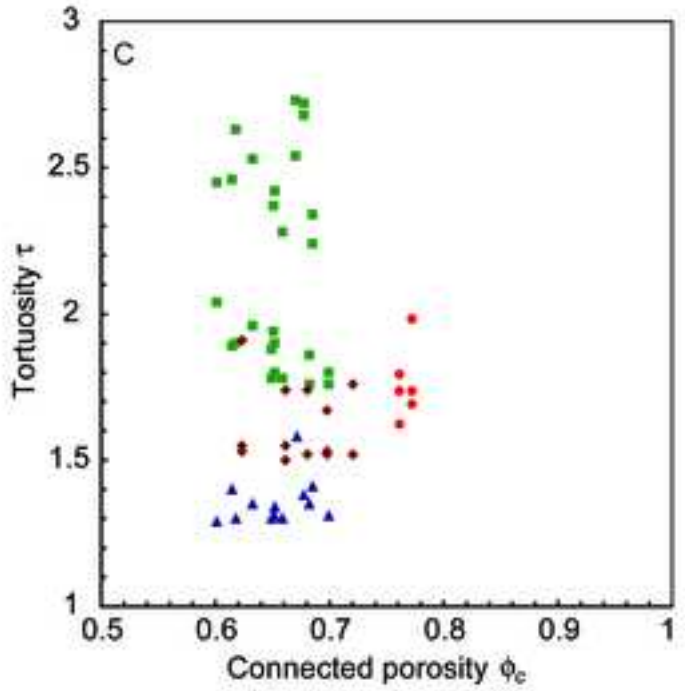
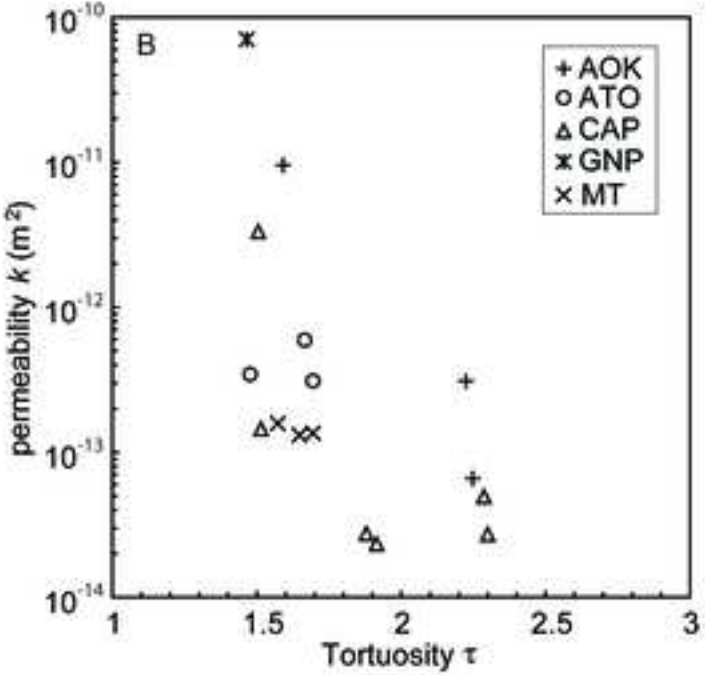
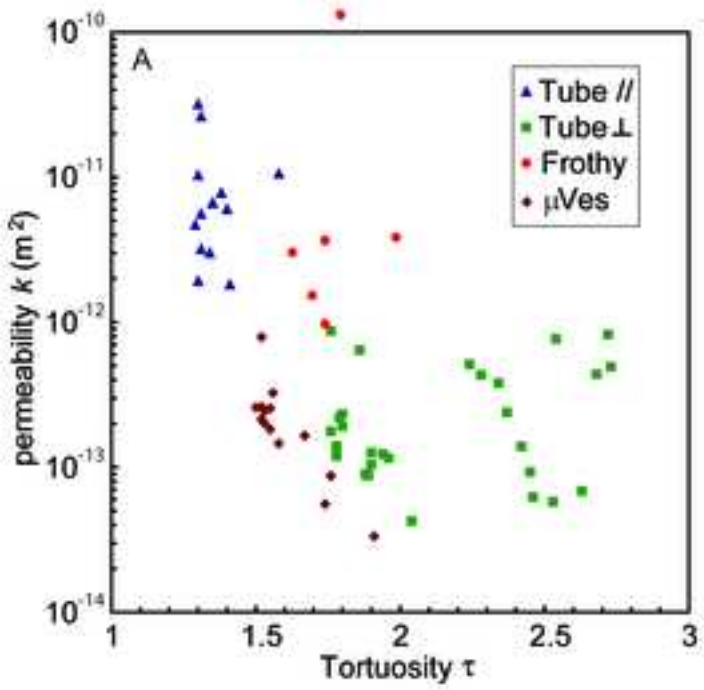


B









permeability k (m^2)

10^{-13}

10^{-12}

10^{-11}

10^{-10}

Tube //



Tube \perp



Frothy



μ Ves



Unit	Origin		Eruption Age	Composition	Reference	
KPT	Kos, Greece	caldera forming	Kos Plateau Tuff, Ignimbrite	160 ky	rhyolite	Allen 2001, Bouvet de Maisonneuve et al. 2009
AOK	Okmok, Alaska	caldera forming	Okmok II, fall deposit	2050 y	rhyodacite	Burgisser 2005, Larsen et al. 2007
ATO	Nevado de Toluca, Mexico	Plinian	Upper Toluca Pumice, flow	10445 y	dacite	Burgisser and Gardner 2006
CAP	Capadocia, Turkey	Plinian	Lower Acigol Tuff, fall deposit	180 ky	rhyolite	Druitt et al. 1995
GNP	Mt Dore, Massif Central, France	caldera forming	Grande Nappe de Ponce, Ignimbrite	2.5 My	rhyolite	Mossand 1983
MT	Mt Pelée, Martinique, Lesser Antilles	Plinian	P3, flow	2010 y	andesite	Martel and Poussineau 2007

deposit	type	clast#	sample#	subvolume#	beamline	analyzed volume (voxels)	voxel size (μm^3)		
KPT	tube	54	A	1	TOMCAT, SLS	512 x 512 x 512	0.74 x 0.74 x 0.74		
				2					
				3					
			C	1				600 x 600 x 600	
				2					
				3					
	D	1	700 x 700 x 700						
		2							
		3							
	μ Ves	43	G	I	1	SYRMEP, ELETTRA	512 x 512 x 512	0.37 x 0.37 x 0.37	
					2		700 x 700 x 700		
					3				
4									
frothy				27	C		450 x 450 x 450		7.74 x 7.74 x 7.74
				32	C		400 x 400 x 400		
AOK		1	A		ID19, ESRF	1024 x 1024 x 1024	0.55 x 0.55 x 0.55		
ATO		42	A						
CAP		67I	A	1					
				2					
GNP		1	A						
MT		37T	A						

sample	ϕ	τ_z	τ_x	τ_y	$k_z (m^2)$	$k_x (m^2)$	$k_y (m^2)$	s (1/ μm)
KPT54A1	0.7	1.41	2.24	2.34	1.82E-012	5.12E-013	3.80E-013	8.61E-002
KPT54A2	0.7	1.58	2.54	2.73	1.06E-011	7.67E-013	4.93E-013	8.55E-002
KPT54A3	0.7	1.38	2.72	2.68	7.78E-012	8.21E-013	4.38E-013	8.56E-002
KPT54C1	0.65	1.31	2.37	1.94	5.58E-012	2.38E-013	1.23E-013	5.46E-002
KPT54C2	0.6	1.29	2.45	2.04	4.67E-012	9.27E-014	4.25E-014	5.49E-002
KPT54C3	0.66	1.3	2.28	1.78	3.19E-011	4.32E-013	1.40E-013	5.46E-002
KPT54D1	0.66	1.34	1.79	2.42	3.00E-012	2.20E-013	1.39E-013	3.48E-002
KPT54D2	0.62	1.3	1.9	2.63	1.92E-012	1.04E-013	6.84E-014	3.49E-002
KPT54D3	0.64	1.35	1.96	2.53	6.61E-012	1.16E-013	5.78E-014	3.51E-002
KPT54D4	0.62	1.4	1.89	2.46	6.01E-012	8.77E-014	6.23E-014	3.48E-002
KPT54I1	0.68	1.35	1.76	1.86	6.68E-012	8.71E-013	6.44E-013	8.68E-002
KPT54I2	0.65	1.31	1.8	1.9	3.19E-012	1.91E-013	1.26E-013	3.49E-002
KPT54I3	0.7	1.31	1.8	1.76	2.63E-011	2.32E-013	1.77E-013	3.48E-002
KPT54I4	0.65	1.3	1.88	1.78	1.03E-011	8.96E-014	1.20E-013	3.50E-002
KPT43G1	0.7	1.67	1.52	1.53	1.65E-013	2.61E-013	2.45E-013	1.73E-001
KPT43G2	0.62	1.91	1.53	1.55	3.34E-014	2.01E-013	1.83E-013	1.74E-001
KPT43G3	0.66	1.74	1.5	1.55	5.56E-014	2.59E-013	2.55E-013	1.74E-001
KPT43G4	0.68	1.74	1.52	1.58	5.57E-014	2.15E-013	1.46E-013	1.74E-001
KPT43G5	0.72	1.76	1.52	1.56	8.71E-014	7.90E-013	3.26E-013	1.73E-001
KPT27c	0.79	1.74	1.98	1.69	9.30E-013	9.77E-013	3.88E-013	3.43E-002
KPT32c	0.77	1.74	1.62	1.79	2.47E-013	7.67E-013	2.91E-011	2.41E-002
AOK1A	0.78	1.59	2.25	2.22	9.56E-012	6.58E-014	3.09E-013	1.65E-002
ATO42A	0.70	1.7	1.48	1.67	3.10E-013	3.45E-013	5.93E-013	1.94E-002
CAP67IA1	0.60	1.51	2.3	1.92	1.45E-013	2.72E-014	2.33E-014	1.86E-002
CAP67IA2	0.63	1.51	2.29	1.88	3.33E-012	4.96E-014	2.75E-014	1.85E-002
GNP1A	0.73	1.47	-	-	7.04E-011	0	0	1.48E-002
MT37TA	0.52	1.69	1.65	1.57	1.35E-013	1.32E-013	1.58E-013	1.90E-002

